Pejman Hadi Sichani
Department of Engineering and Architecture (DPIA),
University of Udine,
Udine 33100, Italy;
Institute of Fluid Mechanics and Heat Transfer,
Vienna University of Technology,
Vienna 1060, Austria
e-mails: pejman.sichani@tuwien.ac.at;
hadisichani.pejman@spes.uniud.it

Cristian Marchioli
Department of Engineering and Architecture (DPIA),
University of Udine,
Udine 33100, Italy,
e-mail: marchioli@uniud.it

Francesco Zonta
Institute of Fluid Mechanics and Heat Transfer,
Vienna University of Technology,
Vienna 1060, Austria,
e-mail: francesco.zonta@tuwien.ac.at

Alfredo Soldati[2]
Institute of Fluid Mechanics and Heat Transfer,
Vienna University of Technology,
Vienna 1060, Austria;
Department of Engineering and Architecture (DPIA)
University of Udine,
Udine 33100, Italy,
e-mail: alfredo.soldati@tuwien.ac.at

Shear Effects on Scalar Transport in Double Diffusive Convection[1]

In this article, we examine the effect of shear on scalar transport in double diffusive convection (DDC). DDC results from the competing action of a stably stratified, rapidly diffusing scalar (temperature) and an unstably stratified, slowly diffusing scalar (salinity), which is characterized by fingering instabilities. We investigate, for the first time, the effect of shear on the diffusive and convective contributions to the total scalar transport flux within a confined fluid layer, examining also the associated fingering dynamics and flow structure. We base our analysis on fully resolved numerical simulations under the Oberbeck–Boussinesq condition. The problem has five governing parameters: The salinity Prandtl number, Pr_s (momentum-to-salinity diffusivity ratio); the salinity Rayleigh number, Ra_s (measure of the fluid instability due to salinity differences); the Lewis number, Le (thermal-to-salinity diffusivity ratio); the density ratio, Λ (measure of the effective flow stratification), and the shear rate, Γ. Simulations are performed at fixed Pr_s, Ra_s, Le, and Λ, while the effect of shear is accounted for by considering different values of Γ. Preliminary results show that shear tends to damp the growth of fingering instability, leading to highly anisotropic DDC dynamics associated with the formation of regular salinity sheets. These dynamics result in significant modifications of the vertical transport rates, giving rise to negative diffusive fluxes of salinity and significant reduction of the total scalar transport, particularly of its convective part. [DOI: 10.1115/1.4048342]

1 Introduction

Double diffusion convection (DDC) is a mixing process driven by the difference in the molecular diffusivities of two scalar fields, such as heat and salt, within a confined fluid layer [1–4]. When a fluid layer experiences an unstable gradient of the slowly diffusing scalar and a stable gradient of the rapidly diffusing scalar, a convective instability can occur: such instability, referred to as fingering convection hereinafter [5], leads to the formation of narrow upgoing and downgoing columns of fluid that develop in the bulk of the flow and favour scalar transport across the layer [6–8]. The resulting flow structure is also characterized by the formation of a thin boundary layer of the slowly diffusing scalar, which superposes to the velocity boundary layer [9]. Because of its relevance in many important applications, ranging from mixing in large water bodies [1,10,11] to electrodeposition cells [12], double-diffusive convection has received a lot of attention since the pioneering works of Stern [13] and Turner [6]. When the diffusing scalars are temperature and salinity, in particular, scaling laws for key parameters of DDC (such as the nondimensional salinity flux, the salinity Rayleigh number, which measures the fluid instability due to salinity differences, and the density ratio of the buoyancy forces induced by two scalar differences) have been derived recently by Yang et al. [9], exploiting a generalization of the Grossmann–Lohse theory originally developed for traditional Rayleigh–Bénard convection [14].

In some situations, for example, buoyant outflows in water bodies, DDC is affected by shear, which can be produced by bulk motion of water masses like those produced by adjacent intruding layers [15–17]. The effect of shear on the growth of double-diffusive convection has been the subject of several studies (from the pioneering work of Linden [18], who focused on eddies impinging upon a density step where salt fingers were growing, to the more recent numerical works by Smyth and Kimura [19,20], Radko et al. [17], and Konopliv et al. [15], and experimental works by Wells et al. [21] and Fernandes and Krishnamurti [22]. The main effect observed in both laboratory and numerical investigations was the alignment of the fingers in the direction of shear, which leads to the formation of sheet-like structures and to a reduction of vertical double-diffusive transport rates compared to those measured in three-dimensional (3D) DDC in the absence of shear [17]. In the plane perpendicular to the direction of shear, however, double diffusion can still produce vertically elongated filaments similar to those observed in zero-shear DDC [17]. It should be noted that most of the numerical investigations of DDC convection in shear flow were conducted using linear stability analysis [16,18], which allows for the identification of the most unstable modes responsible for the onset of convection, or transient growth analysis [15], which was used to identify the maximum perturbation growth of the fingers by means of a suitably defined optimization problem. Only a few studies are based on fully resolved three-dimensional simulations of the flow. In particular, Smyth and Kimura [20] performed direct simulations of DDC in the presence of shear-induced Kelvin–Helmholtz instabilities, whereas Radko et al. [17] examined the case of DDC subject to stochastic shear. We also observe that a precise identification of shear effects on the local diffusive and convective contributions to the total scalar fluxes in the gravity direction is lacking, the

[1]This article is dedicated to the memory of Dr. Malcolm J. Andrews.
[2]Corresponding author.

Contributed by the Fluids Engineering Division of ASME for publication in the Journal of Fluids Engineering. Manuscript received November 1, 2019; final manuscript received March 16, 2020; published online October 29, 2020. Assoc. Editor: Arindam Banerjee.

discussion being focused on the global transport parameters of the flow (e.g., salinity and thermal Nusselt number).

In this work, we quantify the modifications on DDC induced by the superposition of a mean shear, which introduces a symmetry breaking effect into the flow. We also examine the resulting change in the scalar fluxes, determining the relative importance of their diffusive and convective parts. This problem is of relevance in a number of applications [11] and, to the best of our knowledge, is investigated here for the first time. To this aim, we perform fully resolved three-dimensional simulations of DDC within a fluid layer bounded by a solid (no-slip) wall at the bottom and a slip surface (mimicking a nonhomogeneous convection layer associated with an anisotropic scalar distribution) at the top. The effect of a steady shear on fingering formation within a no-slip/slip layer is expected to magnify the asymmetric distribution of the diffusing scalars (temperature and salinity) across the layer, which is due to the fact that horizontal fluid motions are allowed at the slip boundary, yet forbidden at the no-slip boundary. This flow configuration allows us to complement previous studies of DDC between two no-slip walls (see Refs. [12,23–25] among others), or two free-slip walls [10] or between a no-slip wall and a flux-free boundary [20]. Indeed, as demonstrated by Yang et al. [26] for the case of zero-shear vertically bounded DDC in the fingering regime, comparison of different boundary conditions allows deeper physical understanding of fingering dynamics. In addition, our study could provide useful indications regarding the applicability of laboratory experiments, which are usually performed between no-slip walls, and of numerical studies, which use the free-slip condition to approximate an interface in natural environments, to actual DDC flows (like those occurring in water bodies). As mentioned, an important feature of this flow is the contribution to salinity transport given by diffusive and convective mechanisms, which will be analyzed in separation. We will discuss how these two contributions can influence each other and, at the same time, be influenced by the applied shear. We will also show how the resulting complex interplay can lead to interesting phenomena such as the occurrence of local countergradient diffusive fluxes. These may influence the global heat and mass transfer rates leading to quantitative changes in the Nusselt numbers.

The article is organized as follows: In Sec. 2, we describe the numerical methodology adopted to perform the simulations and we summarize the range of simulation parameters covered. Section 3 discusses the flow structure and the observed fingering dynamics first, complementing this phenomenological description with a statistical characterization of velocity, temperature, and salinity distributions as well as heat and salinity fluxes. Section 4 concludes the paper.

2 Methodology

2.1 Physical Problem and Governing Equations. We consider the problem of DDC in a horizontal layer bounded by a no-slip bottom wall and a slip top surface that are orthogonal to gravity (pointing downwards) and are separated by a distance $2h^*$. Note that the superscript $*$ indicates variable in physical units. The flow, which is incompressible and Newtonian, is driven by the competition between the stabilizing distribution of temperature and the destabilizing distribution of salinity. We define the temperature and salinity difference across the fluid layer as $\Delta s^* = s^*_{\text{top}} - s^*_{\text{bot}}$ and $\Delta\theta = \theta^*_{\text{top}} - \theta^*_{\text{bot}}$, where subscripts top and bot refer to the top and bottom boundary, respectively. Naturally, $\Delta s^* > 0$ and $\Delta\theta^* > 0$. The Oberbeck–Boussinesq (OB) approximation, which prescribes that the fluid density varies linearly with s^* and θ^* as

$$\rho^*(\theta^*, s^*) = \rho^*_{\text{ref}}[1 - \beta^*_\theta\theta^* + \beta^*_s s^*] \tag{1}$$

is assumed in this work. Here, ρ^*_{ref} is the reference density (equal to the density of the fluid at reference temperature and salinity), while β^*_θ and β^*_s are the volumetric thermal and salinity expansion coefficients, respectively. Note that both temperature and salinity are expressed with respect to their reference values $\theta^*_{\text{ref}} = (\theta^*_{\text{bot}} + \theta^*_{\text{top}})/2$ and $s^*_{\text{ref}} = (s^*_{\text{bot}} + s^*_{\text{top}})/2$. For a deeper discussion on the range of applicability of the OB approximation, we refer the reader to Ref. [27]. In dimensionless form, the governing equations that describe the problem are

$$\frac{\partial u_i}{\partial x_i} = 0 \tag{2}$$

$$\frac{\partial u_i}{\partial t} + u_j\frac{\partial u_i}{\partial x_j} = -\frac{\partial p}{\partial x_i} + \sqrt{\frac{\text{Pr}_\text{s}}{\text{Ra}_\text{s}}}\frac{\partial^2 u_i}{\partial x_j^2} + \delta_{iz}(\Lambda\theta - s) \tag{3}$$

$$\frac{\partial\theta}{\partial t} + u_j\frac{\partial\theta}{\partial x_j} = \text{Le}\sqrt{\frac{1}{\text{Pr}_\text{s}\text{Ra}_\text{s}}}\frac{\partial^2\theta}{\partial x_j^2} \tag{4}$$

$$\frac{\partial s}{\partial t} + u_j\frac{\partial s}{\partial x_j} = \sqrt{\frac{1}{\text{Pr}_\text{s}\text{Ra}_\text{s}}}\frac{\partial^2 s}{\partial x_j^2} \tag{5}$$

where u_i is the ith component of the velocity, p is the kinematic pressure, while δ_{iz} is the Kronecker delta used to account for the buoyancy term in the vertical direction only. The dimensionless numbers that appear in Eqs. (2)–(5) are the Lewis number Le, the density ratio Λ, the salinity Rayleigh number Ra_s, and the salinity Prandtl number Pr_s. These are defined as

$$\text{Ra}_\text{s} = \frac{g^*\beta^*_s\Delta s^*(2h^*)^3}{\kappa^*_s\nu^*}, \quad \text{Pr}_\text{s} = \frac{\nu^*}{\kappa^*_s}, \quad \text{Le} = \frac{\kappa^*_\theta}{\kappa^*_s}, \quad \text{and} \quad \Lambda = \frac{\beta^*_\theta\Delta\theta^*}{\beta^*_s\Delta s^*}$$

where g^* is the gravity acceleration, ν^* is the kinematic viscosity while κ^*_θ and κ^*_s are the thermal and salt diffusivities, respectively [24]. A further parameter that controls the flow is the imposed shear. In dimensionless form, it is defined as

$$\Gamma = \frac{u^*_\text{m}}{U^*} \tag{6}$$

where u^*_m is the imposed mean velocity at the top boundary and U^* is a suitable reference velocity scale for the DDC process. In convection–diffusion problems, we can define one velocity scale based on convection and one based on diffusion. The most common choice one can find in the literature is to scale all velocities by the free-fall velocity of the convective plumes, defined as $U^* = \sqrt{g^*\beta^*_s h^*(\Delta s^*/2)}$. The alternative option is to use the diffusive velocity scale $U^*_\text{d} = \kappa^*_\theta/d^*$, where

$$d^* = \left(\frac{\kappa^*_\theta\nu^*}{g^*\beta^*_\theta\dfrac{\partial\langle\theta^*\rangle}{\partial z^*}}\right)^{\frac{1}{4}} \tag{7}$$

is the characteristic diffusive length scale of the problem [1]. As a consequence, the dimensionless shear velocity reads as

$$\Gamma_\text{d} = \frac{u^*_\text{m}d^*}{\kappa^*_\theta} \tag{8}$$

In this particular problem, transport parameters are such that the heat transfer is dominated by diffusion, thus leading the temperature gradient to attain a constant value, which in dimensionless units is $\partial\langle\theta\rangle/\partial z \simeq 1$. Therefore, we obtain

$$\frac{\Gamma_\text{d}}{\Gamma} = \frac{1}{2}\left(\frac{\text{Ra}_\text{s}\text{Pr}_\theta^2}{\text{Le}\Lambda}\right)^{\frac{1}{4}} \tag{9}$$

To discuss the statistics of velocity, temperature, and salinity shown in Sec. 3.2, we will refer to Γ, and we will exploit the diffusive scaling to discuss the fundamental transport mechanisms examined in Sec. 3.3.

2.2 Numerical Details and Simulation Parameters. In this section, we briefly summarize the main numerical details of the proposed simulations. The dimensionless set of conservation equations, Eqs. (2)–(5), are discretized using a pseudospectral method, based on transforming the field variables into wavenumber space via Fourier series and Chebyshev expansions in the homogeneous (periodic) and in the wall-normal directions, respectively. To maintain the spectral accuracy and at the same time to increase the computational efficiency, derivatives are evaluated directly in the wavenumber space, whereas nonlinear terms are computed in the physical space and then transformed to the wavenumber space using a two-thirds dealiasing rule. Time advancement is achieved using an implicit Crank–Nicolson scheme for the diffusive (linear) terms, and an explicit Adams–Bashforth scheme for the convective (nonlinear) terms. Further details on the numerical method can be found in Ref. [28]. The imposed boundary conditions are as follows. Dirichlet boundary conditions are enforced at the top and bottom boundaries for temperature (θ^*_{bot} and θ^*_{top}) and salinity (s^*_{bot} and s^*_{top}). The application of a shear is realized by imposing a mean horizontal velocity u^*_{m} at the top boundary, and a no-slip condition at the bottom boundary. More specifically, at the top boundary, we impose that both mean and fluctuating components of the wall-normal fluid velocity are zero (no penetration through the upper slip surface), but we allow fluctuations of the streamwise and spanwise velocities, thus ensuring mass conservation. Note that, for the horizontal velocity components, only the mean value is imposed (equal to the applied shear velocity in the streamwise direction and to zero in the spanwise direction). Periodicity is applied for all variables along the homogeneous directions x and y.

Present simulations are run at $\text{Ra}_s = 10^7$, $\Lambda = 1$, $\text{Pr}_\theta = 7$, and $\text{Pr}_s = 700$, which yield $\text{Le} = 100$ and from Eq. (9), $\Gamma_d \simeq 23.5\Gamma$. Three different values of the dimensionless shear velocity are chosen: $\Gamma = 0$, $\Gamma = 0.02$, and $\Gamma = 0.1$, corresponding to $\Gamma_d = 0$, $\Gamma_d \simeq 0.47$, and $\Gamma_d \simeq 2.35$, respectively. The domain, whose dimensions are $4\pi h^* \times 2\pi h^* \times 2h^*$, is longer in the streamwise direction to cope with the applied shear. The spatial grid is composed by $1024 \times 512 \times 513$ nodes along x, y, and z, respectively, and has been chosen to capture the thin salinity boundary layers. Validation of the grid resolution is provided in the Appendix. All the simulations start from a zero-velocity (hydrostatic) initial condition. At the beginning of the simulation, salinity has a uniform distribution equal to $(s_{\text{top}} + s_{\text{bot}})/2$, while temperature is distributed linearly across the fluid layer (between the values θ_{top} and θ_{bot}). The same initial conditions were chosen by Yang et al. [9], which are in turn similar to those considered in the experiments by Hage and Tilgner [23] and by Kellner and Tilgner [12] for the zero-shear case. Note that small random perturbations of both the salinity and the temperature fields have been applied to accelerate the flow development over time.

3 Results

In this section, the results of the numerical simulations are presented and discussed. The structure of the flow is first analyzed from a qualitative viewpoint (Sec. 3.1) and then from a quantitative viewpoint described by statistical moments (Sec. 3.2) and transport fluxes (Sec. 3.3). Although statistics have been computed for all three values of Γ, the effects of shear we wish to discuss are magnified for the case with $\Gamma = 0.1$. For this reason, in the following sections, we will show results at $\Gamma = 0.02$ only when they add to the discussion.

3.1 Phenomenology of Double Diffusive Convection Fingering. We start our analysis by looking at the instantaneous flow structure. A three-dimensional rendering of salinity isosurfaces, and the associated two-dimensional (2D) maps of salinity contours are shown in Fig. 1 for $\Gamma = 0$ (left column: Figs. 1(*a*)–1(*d*)) and for $\Gamma = 0.1$ (right column: Figs. 1(*e*)–1(*h*)). The flow structure for $\Gamma = 0.02$ (not shown in the figure) exhibits an intermediate behavior between those shown. Salinity contours are measured on horizontal slices located at $z \equiv z^*/h^* = -0.95$, $z = 0$ and $z = 0.95$, respectively. We look first on the zero-shear case, and we focus on Fig. 1(*a*). Thin salt fingers of heavy and light fluids are emitted from the top and bottom boundaries, travel over the entire vertical extension of the fluid layer and reach the opposite boundary. The shape and the distribution pattern of these fingers is such that heavy and light fingers come one after the other and define the boundaries of adjacent and vertically elongated convection cells. The qualitative structure of the flow is similar to that observed in the classical configuration with two no-slip boundaries [9,29] although the different boundary conditions prescribed here (slip conditions at the top, and no-slip conditions at the bottom) induce a slight asymmetry, with fingers emerging from the top boundary being a bit stronger than those emerging from the bottom boundary. The main reason for this asymmetry is that all components of the fluid velocity must go to zero at the bottom boundary, while horizontal motions are possible—but vertical motions forbidden—at the top boundary (vertical geometrical constraint). As a consequence, the flow recirculation close to the upper portion of the fluid layer is stronger compared to that occurring in the lower portion of the layer [26]. To analyze the organized flow structure of salt fingers more closely, we focus now on the two-dimensional contour maps of salinity in Figs. 1(*b*)–1(*d*). Near the bottom and top boundaries (Figs. 1(*b*)–1(*d*)), we observe the presence of thin branches (sheet-like structures) characterized by different orientations and connected in such a way that they form a regular network of polygonal-shape cells. At the bottom boundary (Fig. 1(*b*)), these thin branches are characterized by low salinity (rendered as blue isocontours). Intense blue spots appear at the intersection between neighboring branches, and represent the root of light fingers that move vertically upward. At the same time, dense fingers (rendered as red regions of salty fluid in Fig. 1) move close to the bottom boundary to replace the fluid transported away by upward-moving fingers (fluid eruptions). Since temperature diffusion mechanisms are two orders of magnitude faster than salinity diffusion mechanisms, temperature horizontal gradients are quickly equalized while fingers travel upward, and the flow field can be considered in thermal equilibrium over horizontal planes. It is therefore solely the salinity difference that produces the buoyancy forces driving the fingers upward. But, since salt convection is in this instance stronger than salt diffusion, such buoyancy forces maintain fingers coherency and drive them across the fluid layer, up to the top boundary. Here, the fluid becomes progressively denser and accumulates (red branches connected by red spots) until there is a thick enough layer of dense fluid for a new finger to form. Each finger travels the entire fluid layer and generates a stable *jet* of fluid close to the opposite boundary. Upon impingement with such boundary, fingers are deflected in the horizontal direction and lose their coherence. The deflection of fingers generates a strong divergence of the horizontal velocity field near the boundary, which collects fluid into specific regions (thin branches converging toward spots) from which fingers with opposite buoyancy are emitted. From a vis-à-vis comparison of Fig. 1(*b*) with Fig. 1(*d*), we note that the pattern of branches at the bottom boundary is more organized than the one at the top boundary, due to the different boundary conditions. Also, the extremely organized pattern of structures observed near the boundaries is replicated at the center of the fluid layer (Fig. 1(*c*)) in the form of a sequence of alternating fingers (round-shaped structures) of heavy and light fluids, rendered in red and blue, respectively.

When the mean shear $\Gamma = 0.1$ is applied at the top boundary, the situation changes remarkably. This is visualized in the right column of Figs. 1(*e*)–1(*h*). By looking at the 3D maps of salinity (Fig. 1(*e*)), it is apparent that salt fingers are inclined by the mean shear and lose the strong vertical coherence observed for $\Gamma = 0$ in Fig. 1(*a*). This is even more visible by looking at the 2D contour maps of salinity measured at the three different vertical locations (Figs. 1(*f*)–1(*h*)). Close to the bottom boundary (Fig. 1(*f*)), we still observe the presence of thin, sheet-like branches, which however

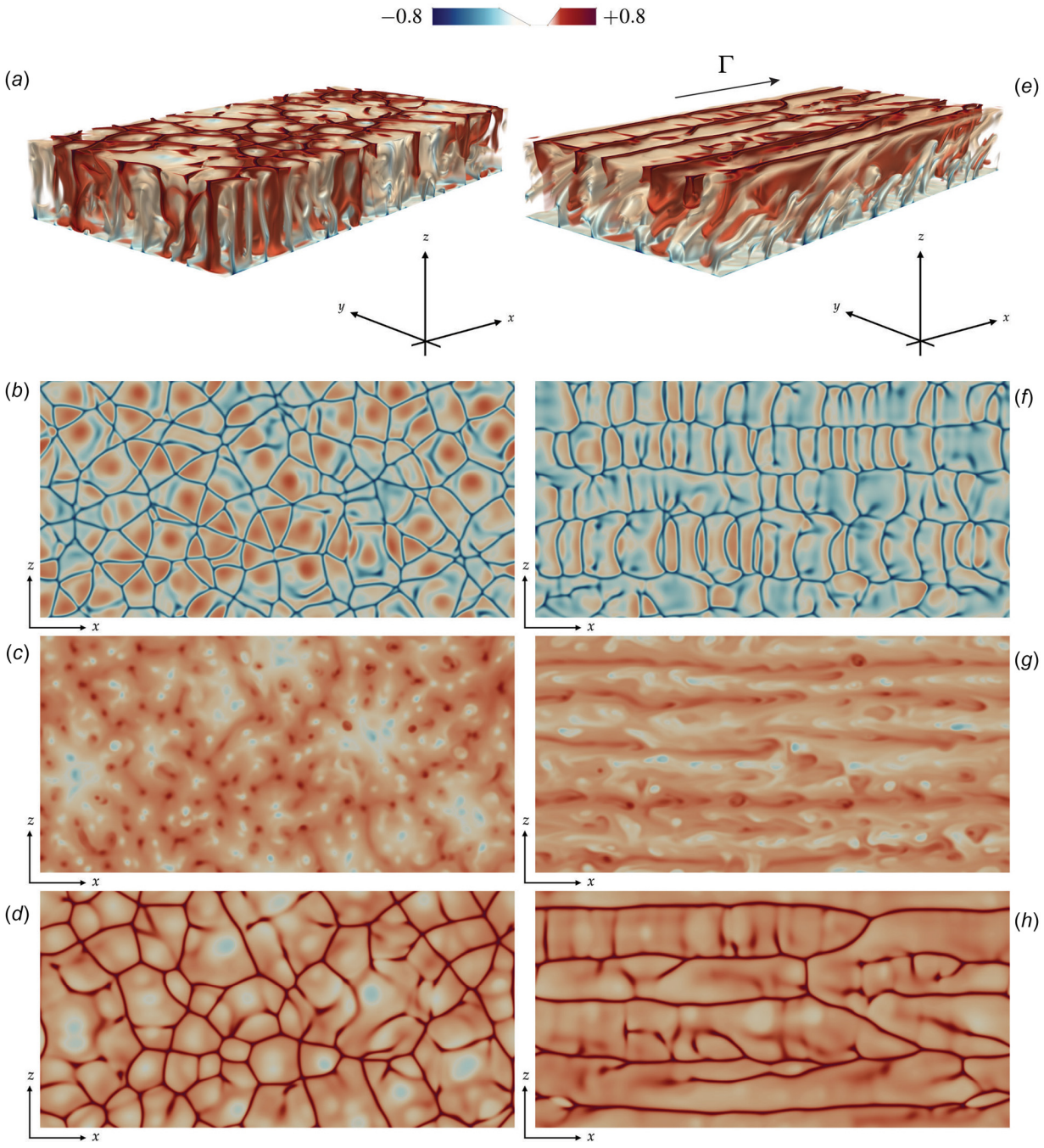

Fig. 1 Three-dimensional volume rendering, and associated two-dimensional maps, of salinity distribution for (*a*)–(*d*) $\Gamma = 0$ and (*e*)–(*h*) $\Gamma = 0.1$. Two dimensional maps are measured at $z = -0.95$ ((*b*) and (*f*) i.e., close to the bottom boundary), $z = 0$ ((*c*) and (*g*) i.e., at the cell center) and $z = 0.95$ ((*d*) and (*h*) i.e., close to the top boundary). For all panels, the same colormap but different opacity settings are used, with red indicating high-salinity (dense) fluid, and blue indicating low-salinity (light) fluid. An opacity filter is used for the volume rendering, whereas a standard sequential colormap is used for the two-dimensional maps.

form long chains aligned with the direction of the imposed shear. Shorter braids, orthogonal to the direction of shear, connect the different horizontal chains. A similar pattern, though less organized and coherent, is observed close to the top boundary (Fig. 1(*h*)), and is somehow maintained also at the center of the fluid layer (Fig. 1(*g*)). This dramatic change of the flow structure will reflect on the corresponding statistics, as discussed in Secs. 3.2 and 3.3.

3.2 Statistical Moments of Velocity, Temperature, and Salinity. The profiles of dimensionless salinity, $\langle s(z) \rangle$; temperature, $\langle \theta(z) \rangle$; and axial velocity $\langle u_x(z) \rangle$ are shown in Fig. 2, as a function of the distance from the bottom boundary, z, for $\Gamma = 0$ and $\Gamma = 0.1$. Angular brackets indicate averaging in time and over the horizontal x–y plane. Profiles for $\Gamma = 0.02$ are not included since they always fall in between those shown and, therefore, do not add to the discussion. Salinity, temperature, and velocity are defined as

$$\theta = \frac{\theta^* - \theta^*_{\text{ref}}}{\frac{\Delta\theta^*}{2}}, \quad s = \frac{s^* - s^*_{\text{ref}}}{\frac{\Delta s^*}{2}}, \quad u = \frac{u^*}{\sqrt{g^* \beta^*_s h^* (\Delta s^*/2)}}$$

The time-averaging window, in dimensionless form, is defined as $T_{\text{avg}} = T^*_{\text{avg}}/(h^*/U^*)$, where T^*_{avg} is the time window in

physical units and h^*/U^* is the time scale associated with the free-fall velocity U^*. The values of T_{avg} considered in each simulation are 2200, 2700, and 3000 for $\Gamma = 0$, $\Gamma = 0.02$ and $\Gamma = 0.1$, respectively. Note that all observables examined in this paper refer to statistically steady flow conditions. We consider first the case $\Gamma = 0$ (Fig. 2(*a*)). As expected, we find that $\langle u_x(z)\rangle = 0$. Also expected is the linear profile of the mean temperature, $\langle\theta(z)\rangle$, which is typical of a diffusion-dominated process: This is clearly the case of temperature, which has a large diffusion coefficient and diffuses very efficiently. What is nontrivial is the behavior of the mean salinity $\langle s(z)\rangle$. First, $\langle s(z)\rangle$ is not symmetric, due to the asymmetric velocity boundary conditions. We also notice that the mean salinity changes very rapidly close to the boundaries. This marks the presence of two thin boundary layers, which however seem to differ in thickness. Because of the different boundary conditions, the bottom boundary layer seems thicker than the top one. A more quantitative evaluation of the boundary layer thickness will be given below, based on the behavior of the salinity fluctuations. In the core region of the fluid layer, for $0.5 < z < 1.5$, the mean salinity is almost constant and equal to $\langle s\rangle \simeq 0.15$. Interestingly, the profile of the mean salinity is nonmonotonic and develops a local minimum in the region $1.5 < z < 2$ as well as a local maximum in the region $0 < z < 0.5$. This nonmonotonic behavior has important consequences for the global heat and salinity transfer rates, which will be discussed in Sec. 3.3. Considering the $\Gamma = 0.1$ case, the global picture does not change much compared to the $\Gamma = 0$ case (in particular for $\langle s\rangle$ and $\langle\theta\rangle$), the only obvious difference being the profile of the mean horizontal velocity, which exhibits a linear behavior between the values $\langle u_x\rangle = 0$ at the bottom wall and $\langle u_x\rangle = 0.1$ at the top boundary.

To understand further, the different salinity and temperature distributions induced by shear, we look at the behavior of the root-mean-square (RMS) of their fluctuations, $\langle\theta_{rms}\rangle$ and $\langle s_{rms}\rangle$. The RMS of salinity and temperature are computed as

$$\langle\zeta_{rms}\rangle = \sqrt{(\zeta - \langle\zeta\rangle)^2}$$

with $\zeta = \theta, s$. Results are presented in Fig. 3. Open symbols refer to the case $\Gamma = 0$, while filled symbols refer to the case $\Gamma = 0.1$. Again, curves for $\Gamma = 0.02$ are not included as they would fall in between those shown in the figure. Differences in the horizontal and vertical components of the velocity field are also not shown because they are rather small and hence negligible. Fluctuations of temperature (Fig. 3(*a*)) are relatively small and reach their maximum value ($\simeq 9\%$ of the temperature at the boundary) at the center of the fluid layer. The action of a mean shear does not modify qualitatively the shape of the profile, but induces a general attenuation of the fluctuations ($\simeq 6\%$ of the temperature at the boundary). Focusing on the salinity fluctuations (Fig. 3(*b*)), we note that, regardless of the value of Γ, they are much larger than temperature fluctuations, and reach a maximum very close to the boundary ($\simeq 25\%$ of the salinity at the boundary). It is interesting to note that there is a slight asymmetry in the profile of $\langle s_{rms}\rangle$ for both values of Γ, with salinity fluctuations being larger close to the bottom boundary. The action of a mean shear induces a general reduction of solute fluctuations, but does not change qualitatively the shape of the profile. The location at which fluctuations peak is used to estimate the thickness $\lambda \equiv \lambda^*/h^*$ of the boundary layer. For $\Gamma = 0$, $\lambda = 3.133 \times 10^{-2}$ at the bottom wall and $\lambda = 2.243 \times 10^{-2}$ at the top wall, while for $\Gamma = 0.1$, we have

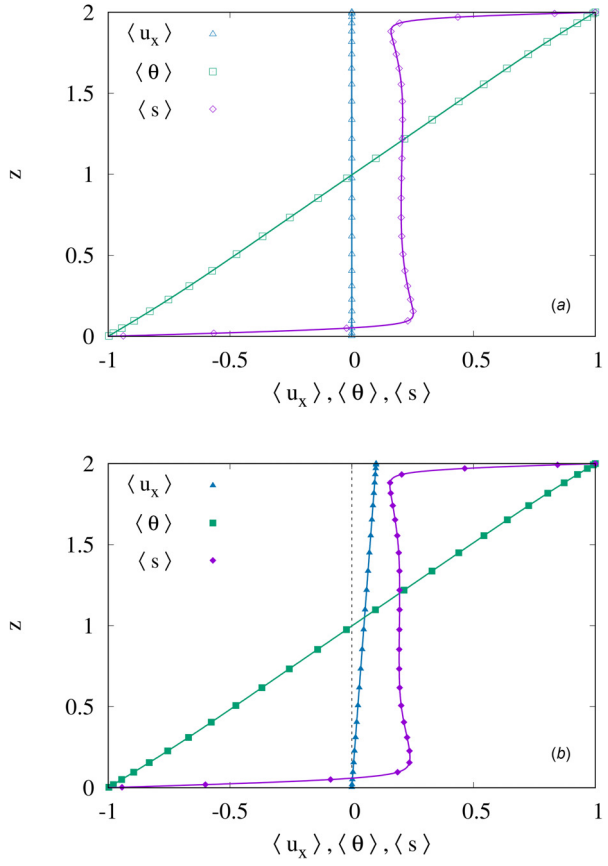

Fig. 2 Profile of the mean salinity, $\langle s\rangle$, mean temperature, $\langle\theta\rangle$, and mean horizontal velocity, $\langle u_x\rangle$, as a function of the vertical distance from the bottom boundary, *z*, for $\Gamma = 0$ (*a*) and $\Gamma = 0.1$ (*b*). The vertical dotted line in (*b*) (zero line) is added for clarity.

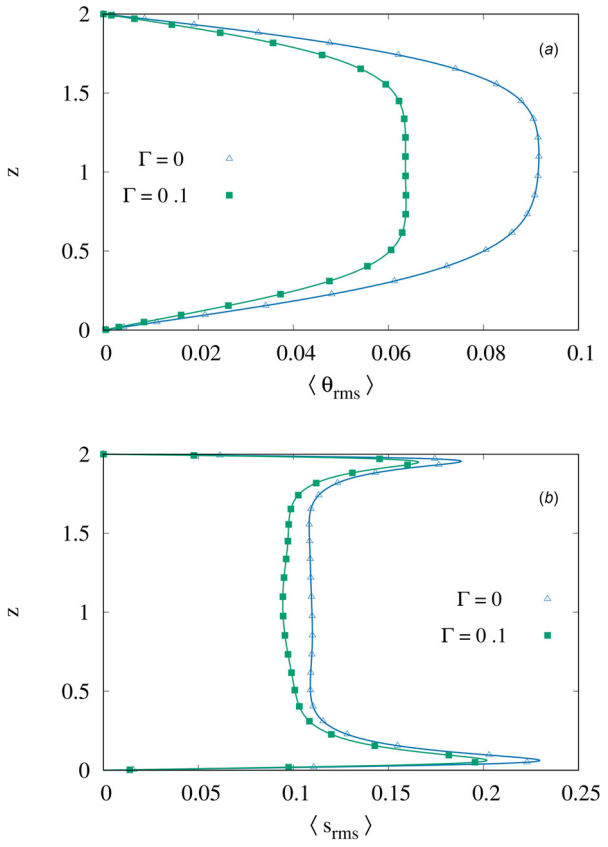

Fig. 3 Profile of the RMS of temperature fluctuations, $\langle\theta_{rms}\rangle$ (*a*), and of salinity fluctuations, $\langle s_{rms}\rangle$ (*b*), as a function of the vertical distance from the bottom boundary, *z*, for $\Gamma = 0$ and $\Gamma = 0.1$, respectively

again $\lambda = 3.133 \times 10^{-2}$ at the bottom wall but $\lambda = 2.523 \times 10^{-2}$ at the top wall. The slight increase of the boundary layer thickness at the top wall resulting from the application of the mean shear indicates a weaker vertical salinity transport, as will be discussed later.

3.3 Heat and Salinity Flux. The different flow behavior induced by shear at the top boundary is expected to influence also the transport rates of heat and salinity. The total heat and salinity fluxes read as

$$q_\theta = \left(\frac{1}{16}\frac{\mathrm{Ra_s Pr}_\theta}{\mathrm{Le}}\right)^{\frac{1}{2}} \langle u_z\theta\rangle - \frac{\partial\langle\theta\rangle}{\partial z}, \quad q_s = \left(\frac{1}{16}\mathrm{Ra_s Pr_s}\right)^{\frac{1}{2}} \langle u_z s\rangle - \frac{\partial\langle s\rangle}{\partial z} \tag{10}$$

and are the sum of a convective contribution (proportional to $\langle u_z\theta\rangle$ and $\langle u_z s\rangle$, respectively) and a diffusive contribution (proportional to $\partial\langle\theta\rangle/\partial z$ and $\partial\langle s\rangle/\partial z$, respectively). The behavior of q_θ and q_s as a function of the vertical coordinate z is shown in Figs. 4 and 5, respectively. We focus first on q_θ (Fig. 4), for the case $\Gamma = 0$. The diffusive and convective components of the total flux are shown using different symbols. In addition, to visualize better their behavior, only a portion of the x-axis is shown. It is apparent that the diffusive heat flux is slightly larger that unity close to the boundaries, $\partial\langle\theta\rangle/\partial z \simeq 1.1$, and slightly smaller than unity at the center of the fluid layer, $\partial\langle\theta\rangle/\partial z \simeq 0.97$. Overall, the departure from a purely diffusive profile, which would correspond to $\partial\langle\theta\rangle/\partial z = 1$, is mild. To counterbalance this temperature anomaly, and to give the expected uniform and constant value of q_θ (vertical dashed line $q_\theta \simeq 1.11$), the convective heat flux is maximum, and approximately constant at the center of the fluid layer, $(\frac{1}{16}\frac{\mathrm{Ra_s Pr}_\theta}{\mathrm{Le}})^{\frac{1}{2}}\langle u_z\theta\rangle \simeq 0.15$. The application of the mean shear at the top boundary induces only negligible changes of both $\langle u_z\theta\rangle$ and $\partial\langle\theta\rangle/\partial z$, and gives an overall heat flux that is only 1% lower than that measured for $\Gamma = 0$ for both $\Gamma = 0.02$ and $\Gamma = 0.1$. We turn now to the behavior of the salinity flux q_s (Fig. 5), and on its diffusive and convective parts, starting from the case $\Gamma = 0$. The diffusive part $\partial\langle s\rangle/\partial z$, which measures the steepness of the salinity gradient in the vertical direction, is very large close to the boundaries, but drops down abruptly (it is already close to zero at a distance of $\Delta z \simeq 0.1$ from the boundaries. Interestingly, salinity gradients become negative, as shown in the two left-hand insets of Fig. 5. A negative diffusive flux indicates the existence of regions of the flow where the local mean salinity gradient is opposite to the imposed one (countergradient regions). This may be ascribed to the low diffusivity of salinity, and to the fact that vertical fingers carry their salinity almost unchanged throughout the entire height of the fluid layer. As a consequence, there are regions close to the bottom boundary in which the salinity is that characteristic of the top boundary, and viceversa, thereby inducing the local salinity inversion. The behavior of the convective part of the total flux is complementary to the diffusive one: Large values of $\langle u_z s\rangle$ are observed throughout the entire fluid layer but in the region near the boundaries, where the convective part drops to zero. When summed up together, the diffusive and the convective parts give a total salinity flux that is uniform and constant (see vertical dashed line $q_s \simeq 23$). Considering the $\Gamma = 0.02$ and $\Gamma = 0.1$ cases, we immediately observe that, while the diffusive part is almost unaffected by the imposed shear, the convective part is remarkably reduced (although its shape is qualitatively similar). This behavior has of course an influence on the total salinity flux, which becomes smaller (vertical dashed line at $q_s \simeq 22$ for $\Gamma = 0.02$ and $q_s \simeq 21$ for $\Gamma = 0.1$).

In dimensionless form, and integrated over the entire domain, the heat and salinity fluxes yield the temperature and salinity Nusselt numbers

$$\mathrm{Nu}_\theta = \frac{1}{2}\int_0^2 q_\theta dz, \quad \mathrm{Nu_s} = \frac{1}{2}\int_0^2 q_s dz \tag{11}$$

which are the most important output parameters (i.e., global responses) of the considered physical systems. In Fig. 6, we show the behavior of $\mathrm{Nu_s}$, normalized by its reference value $\mathrm{Nu_{s,0}}$ computed at zero shear, as a function of the applied shear rate, indicated as Γ in the bottom horizontal axis and as Γ_d in the top horizontal axis. The values of $\mathrm{Nu_s}$ are also explicitly given in the table inside Fig. 6, together with the values of Nu_θ, which undergo a negligible change (within 1%) and hence are not directly plotted. The dashed line fitting the numerical results is used here just for the purpose of indicating the trend of $\mathrm{Nu_s}$ with respect to the shear rate. We observe that the salinity flux $\mathrm{Nu_s}/\mathrm{Nu_{s,0}}$ decreases for increasing Γ. For the smallest value of the imposed shear rate,

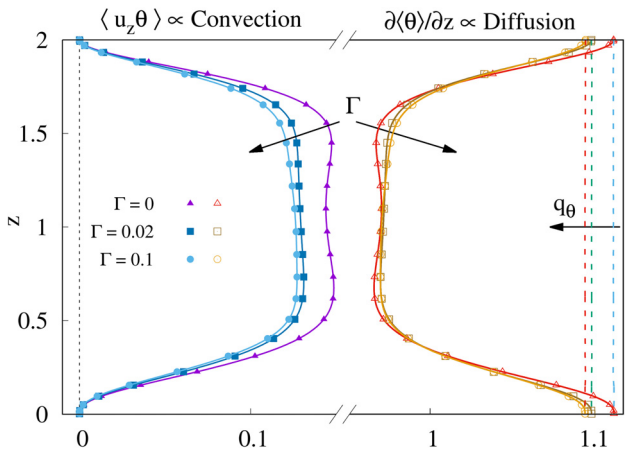

Fig. 4 Vertical behavior of temperature fluxes as a function of the distance from the bottom boundary, z, for $\Gamma = 0$ (triangles), $\Gamma = 0.02$ (squares) and $\Gamma = 0.1$ (circles). Both the convective part ($\sim\langle u_z\theta\rangle$, lines and filled symbols in blue scale) and the diffusive part ($\partial\langle\theta\rangle/\partial z$, lines and open symbols in red scale) to the total heat flux (q_θ, corresponding to the dashed lines on the right-hand side of the plot) are shown. Note that only a portion of the x-axis is shown to emphasize the shear-induced modifications of the fluxes.

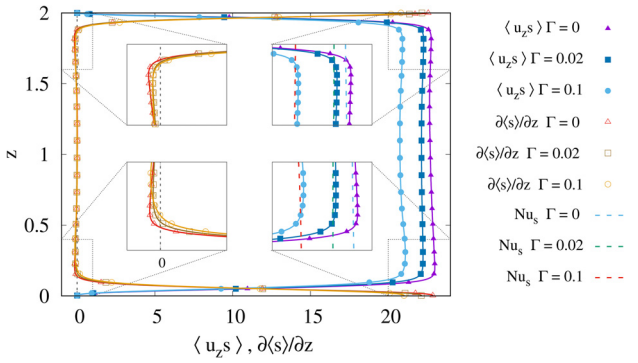

Fig. 5 Vertical behavior of salinity fluxes as a function of the vertical distance from the bottom boundary (z) for $\Gamma = 0$ (triangles), $\Gamma = 0.02$ (squares), and $\Gamma = 0.1$ (circles). Both the convective part ($\langle u_z s\rangle$, lines and filled symbols in blue scale) and the diffusive part ($\partial\langle s\rangle/\partial z$, lines and open symbols in red scale) to the total heat flux (q_s, corresponding to the dashed lines on the right-hand side insets of the plot) are shown. A vertical dotted line (zero line) is also added for clarity. The four insets provide a close-up view of the effect of shear on the salinity fluxes close to the boundaries: The two left-hand insets zoom into the region where the salinity diffusive flux becomes negative and highlight the slight reduction produced by shear; the two right-hand insets zoom in the region where the salinity convective flux flattens and highlight the reduction produced by shear.

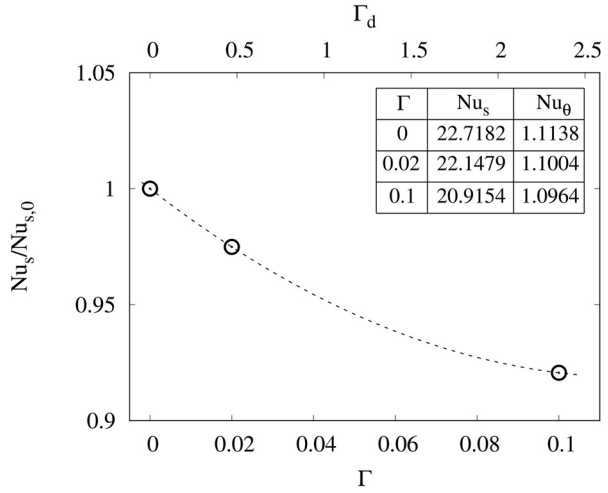

Fig. 6 Salinity Nusselt number Nu_s normalized by Nu_s at $\Gamma = 0$ ($Nu_{s,0}$) as a function of the applied shear rate, indicated as Γ on the bottom horizontal axis and as Γ_d on the top horizontal axis. The table summarizes the values of Nu_s together with the values of the temperature Nusselt number, Nu_θ (not plotted).

$\Gamma = 0.02$, we measure a decrease of about 3% in the vertical salinity flux. The decrease of Nu_s becomes larger (approximately 10%) in the $\Gamma = 0.1$ case. These important modifications in the salinity flux can be discussed also considering the diffusive scaling introduced in Sec. 2.1. The comparison between corresponding values of Γ (which are significantly smaller than unity) and Γ_d (which are of order unity) leads us to hypothesize that indeed diffusive scales are more relevant than the convective scales as far as salinity transport is concerned.

The other important output parameters are the induced flows velocities, customarily measured by the horizontal and vertical Reynolds numbers:

$$\mathrm{Re}_x = \left(\frac{1}{4}\frac{\mathrm{Ra_s}}{\mathrm{Pr_s}}\right)^{\frac{1}{2}}\left(\frac{1}{V}\int u_x^2 dV\right)^{1/2},$$
$$\mathrm{Re}_y = \left(\frac{1}{4}\frac{\mathrm{Ra_s}}{\mathrm{Pr_s}}\right)^{\frac{1}{2}}\left(\frac{1}{V}\int u_y^2 dV\right)^{1/2}, \quad (12)$$
$$\mathrm{Re}_z = \left(\frac{1}{4}\frac{\mathrm{Ra_s}}{\mathrm{Pr_s}}\right)^{\frac{1}{2}}\left(\frac{1}{V}\int u_z^2 dV\right)^{1/2}$$

or, simply, by the overall Reynolds number $\mathrm{Re} = \sqrt{\mathrm{Re}_x^2 + \mathrm{Re}_y^2 + \mathrm{Re}_z^2}$ [12,24]. The value of the horizontal and vertical Reynolds numbers are summarized in Table 1. As expected, and also anticipated by the discussion of Fig. 2, we observe a significant increase of Re_x with Γ, accompanied by a slight increase of Re_y. No monotonic trend is observed for Re_z. However, considering the ratio $\mathrm{Re}_z/\mathrm{Re}_x = u_{z,\mathrm{rms}}/u_{x,\mathrm{rms}}$, we find $\mathrm{Re}_z/\mathrm{Re}_x \simeq 2$ when $\Gamma = 0$ but $\mathrm{Re}_z/\mathrm{Re}_x \simeq 0.15$ when $\Gamma = 0.1$. The decrease of $\mathrm{Re}_z/\mathrm{Re}_x$ reflects a reduction of the vertical convective salinity flux and reveals that the structure of the fingers and their vertical velocity become weaker as the applied shear increases. It is indeed the reduced vertical velocity that weakens the vertical salinity flux, which is the flux influenced by the velocity field: Temperature is essentially dominated by diffusion and remains almost unaltered upon application of the shear.

Table 1 Horizontal and vertical Reynolds numbers as a function of the applied shear rate, Γ

Γ	Re_x	Re_y	Re_z
0	0.28781	0.29117	0.57703
0.02	0.75536	0.32231	0.59546
0.1	3.66565	0.35609	0.56290

4 Conclusions

In this work, we performed fully resolved three-dimensional simulations of double diffusive convection in a confined fluid layer in the fingering regime to examine the influence of shear on heat and salinity transport fluxes: In particular, we focused on the modifications produced by shear on the diffusive and convective contributions to the total flux, which are investigated for the first time. In the present problem, temperature is the rapidly diffusing scalar characterized by a stabilizing distribution across the fluid layer (the top boundary being set at a larger temperature compared to the bottom one), whereas salinity is the slowly diffusing scalar characterized by a destabilizing distribution across the layer (the top boundary being set at a larger salinity compared to the bottom one). To simulate this flow configuration, we considered mixed slip/no-slip boundary conditions: Even in the absence of shear, these produce an asymmetric distribution of the diffusing scalars in the vertical direction that mimics the presence of a nonhomogeneous convection layer. Simulations are run with fixed values of the salinity Rayleigh number $\mathrm{Ra_s} = 10^7$, salinity Prandtl number $\mathrm{Pr_s} = 700$, Lewis number $\mathrm{Le} = 100$, and density ratio $\Lambda = 1$, whereas three different values of shear are considered: $\Gamma = 0$ (corresponding to zero shear), $\Gamma = 0.02$, and $\Gamma = 0.1$ (corresponding to a shearing velocity equal to one-fiftieth and one-tenth of the convective free-fall velocity of the fingers, respectively). In the reference case with zero shear, the flow is dominated by vertical elongated fingers that span the entire height of the fluid layer and transfer efficiently their salt concentration. The application of the shear at the top surface modifies both the size and the structure of the fingers, which appear weaker and aligned with the direction of shear. These flow modifications are found to have an influence on the global heat, salt, and momentum transport. In particular, we document a global decrease of about 10% of the salinity Nusselt number (i.e., the dimensionless salinity transport coefficient) for the $\Gamma = 0.1$ case. Our analysis show that such decrease may be due to the weakening of vertical convective flux observed for increasing Γ.

This study represents a first step toward a deeper understanding of shear effects on scalar transport in DDC. It serves the purposes of assessing an accurate methodology to analyze the complex interplay between diffusive and convective transport mechanisms in DDC, and identifying the key physical parameters of the problem. Further investigations are now required to explore the impact of local countergradient diffusion mechanisms on the global flow parameters over a broader range of values of Γ and, in turn, to derive accurate scaling laws for the scalar transport fluxes.

Acknowledgment

Vienna Scientific Cluster (Vienna, Austria) and CINECA Supercomputing Center (Bologna, Italy) are gratefully acknowledged for generous allowance of computer resources.

Funding Data

- Vienna Scientific Cluster (Vienna, Austria) (71026).
- CINECA Supercomputing Center (Bologna, Italy) (HP10BCFP82).

Nomenclature

d = diffusive length scale
DDC = double diffusive convection
g = gravitational acceleration
h = half height of fluid layer

Le = Lewis number
N_i = number of computational grid points in i direction
Nu_θ = thermal Nusselt number
Nu_s = salinity Nusselt number
OB = Oberbeck–Boussinesq
p = kinematic pressure
Pr_θ = thermal Prandtl number
Pr_s = salinity Prandtl number
q_θ = total heat flux
q_s = total salinity flux
Ra_θ = thermal Rayleigh number
Ra_s = salinity Rayleigh number
Re_i = Reynolds number in i direction
s_{ref} = reference salinity
S = salinity
T_{avg} = time window used to compute statistics
u_i = ith component of the velocity
u_m = imposed shear velocity at the top boundary
U = free-fall velocity
U_d = diffusive velocity

Greek Symbols

β_θ = volumetric thermal expansion coefficient
β_s = volumetric salinity expansion coefficient
Δs = top to bottom salinity difference
$\Delta\theta$ = top to bottom temperature difference
Γ = dimensionless shear velocity (normalized by the free-fall velocity)
Γ_d = dimensionless shear velocity (normalized by the diffusion velocity)
Λ = density ratio
κ_θ = thermal diffusivity
κ_s = salinity diffusivity
θ = temperature
θ_{bot} = temperature at the bottom boundary
θ_{ref} = reference temperature
θ_{top} = temperature at the top boundary
λ_s = thickness of the salinity boundary layer
ρ = density
ρ_{ref} = reference density
ν = kinematic viscosity

Appendix: Validation Case

Validation refers to the case of DDC in a no-slip/no-slip box at $\mathrm{Ra}_s = 10^7$, $\mathrm{Pr}_s = 700$, $\Lambda = 2$, and $\mathrm{Le} = 100$, which replicates one of the cases examined by Yang et al. [9]. In Fig. 7, we show the three-dimensional volume rendering of the (Fig. 7(*a*)) instantaneous flow structure and the associated two-dimensional maps of the

	Present Simulation	Yang et al. [9]
Domain size	$\pi h^* \times \pi h^* \times 2h^*$	$4h^* \times 4h^* \times 2h^*$
Grid Resolution	$512 \times 512 \times 257$	$432 \times 432 \times 240$
Grid spacings	$\Delta x = \Delta y = 3.06 \cdot 10^{-3}$ $\Delta z_{min} = 7.53 \cdot 10^{-5}$ $\Delta z_{max} = 1.22 \cdot 10^{-2}$	$\Delta x = \Delta y = 4.63 \cdot 10^{-3}$ $\Delta z_{min} = 8.64 \cdot 10^{-5}$ $\Delta z_{max} = 1.31 \cdot 10^{-2}$

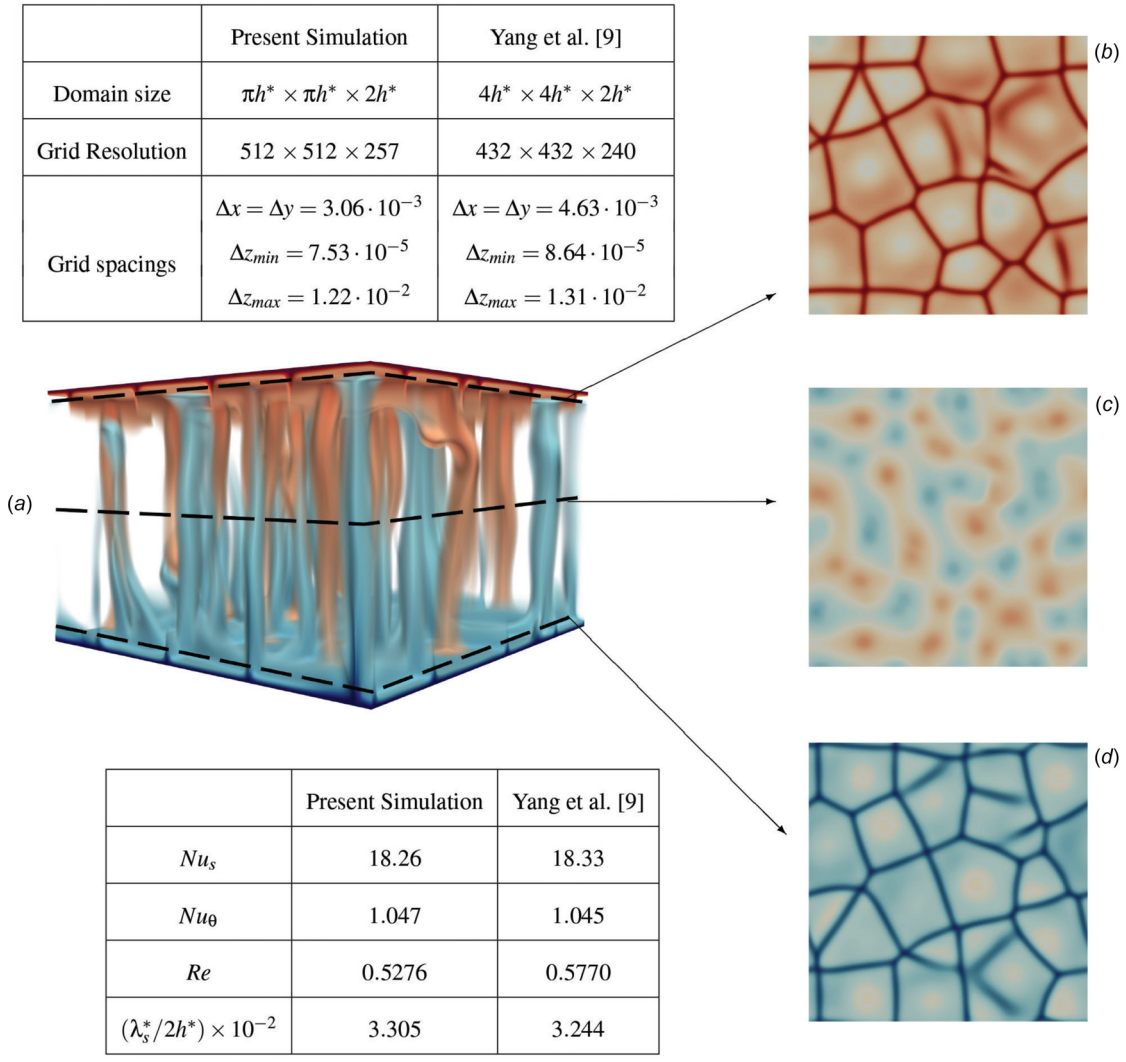

	Present Simulation	Yang et al. [9]
Nu_s	18.26	18.33
Nu_θ	1.047	1.045
Re	0.5276	0.5770
$(\lambda_s^*/2h^*) \times 10^{-2}$	3.305	3.244

Fig. 7 Three-dimensional volume rendering of salinity field (*a*) and the associated two-dimensional maps of salinity distribution, taken at three different locations: (*b*) Near the top boundary ($z = +0.95$); (*c*) at the center ($z = 0$); and (*d*) near the bottom boundary ($z = -0.95$)

salinity distribution, taken at three different locations: (Fig. 7(*b*)) Near the top boundary ($z = +0.95$); (Fig. 7(*c*)) at the center ($z = 0$); and (Fig. 7(*d*)) near the bottom boundary ($z = -0.95$). Tables inside Fig. 7 show a comparison between the domain size and grid resolution of the two simulations, as well as the global response parameters of the flow: salinity Nusselt number, $\mathrm{Nu_s}$, temperature Nusselt number, Nu_θ, Reynolds number, Re, and salinity boundary layer thickness, $\lambda_s^*/2h^*$.

References

[1] Radko, T., 2013, *Double-Diffusive Convection*, Cambridge University Press, New York.

[2] Garaud, P., 2018, "Double-Diffusive Convection at Low Prandtl Number," Annu. Rev. Fluid Mech., **50**(1), pp. 275–298.

[3] Radko, T., and Stern, M., 2000, "Finite-Amplitude Salt Fingers in a Vertically Bounded Layer," J. Fluid Mech., **425**, pp. 133–160.

[4] Schmitt, R. W., 2012, "Finger Puzzles," J. Fluid Mech., **692**, pp. 1–4.

[5] Lee, C., Chang, K., Lee, J. H., and Richards, K. J., 2014, "Vertical Mixing Due to Double Diffusion in the Tropical Western Pacific," Geophys. Res. Lett., **41**(22), pp. 7964–7970.

[6] Turner, J. S., 1967, "Salt Fingers Across a Density Interface," Deep Sea Res., **14**(5), pp. 599–611.

[7] Linden, P. F., 1978, "The Formation of Banded Salt Finger Structure," J. Geophys. Res., **83**(C6), pp. 2902–2912.

[8] Taylor, J., and Bucens, P., 1989, "Laboratory Experiments on the Structure of Salt Fingers," Deep Sea Res., **36**(11), pp. 1675–1704.

[9] Yang, Y., Verzicco, R., and Lohse, D., 2016, "Scaling Laws and Flow Structures of Double Diffusive Convection in the Finger Regime," J. Fluid Mech., **802**, pp. 667–689.

[10] Paparella, F., and Hardenberg, J. V., 2012, "Clustering of Salt Fingers in Double-Diffusive Convection Leads to Staircase Like Stratification," Phys. Rev. Lett., **109**(1), p. 014502.

[11] Sommer, T., Carpenter, J. R., and Wüest, A., 2014, "Double-Diffusive Interfaces in Lake Kivu Reproduced by Direct Numerical Simulations," Geophys. Res. Lett., **41**(14), pp. 5114–5121.

[12] Kellner, M., and Tilgner, A., 2014, "Transition to Finger Convection in Double-Diffusive Convection," Phys. Fluids, **26**(9), p. 094103.

[13] Stern, M. E., 1960, "The Salt-Fountain and Thermohaline Convection," Tellus, **12**(2), pp. 172–175.

[14] Yang, Y., Verzicco, R., and Lohse, D., 2018, "Two-Scalar Turbulent Rayleigh-Bénard Convection: Numerical Simulations and Unifying Theory," J. Fluid Mech., **848**, pp. 648–659.

[15] Konopliv, N., Lesshafft, L., and Meiburg, E., 2018, "The Influence of Shear on Double-Diffusive and Settling-Driven Instabilities," J. Fluid Mech., **849**, pp. 902–926.

[16] Thangam, S., Abdelfattah, Z., and Chen, C. F., 1984, "Salt-Finger Convection in Shear Flow," Phys. Fluids, **27**(4), pp. 804–811.

[17] Radko, T., Ball, J., Colosi, J., and Flanagan, J., 2015, "Double-Diffusive Convection in a Stochastic Shear," J. Phys. Oceanogr., **45**(12), pp. 3155–3167.

[18] Linden, P. F., 1974, "Salt Fingers in a Steady Shear Flow," Geophys. Fluid Dyn., **6**(1), pp. 1–27.

[19] Smyth, W. D., and Kimura, S., 2007, "Instability and Diapycnal Momentum Transport in a Double-Diffusive, Stratified Shear Layer," J. Phys. Oceanogr., **37**(6), pp. 1551–1565.

[20] Smyth, W. D., and Kimura, S., 2011, "Mixing in a Moderately Sheared Salt-Fingering Layer," J. Phys. Oceanogr., **41**(7), pp. 1364–1384.

[21] Wells, M. G., Griffiths, R. G., and Turner, J. S., 2001, "Generation of Density Fine Structure by Salt Fingers in a Spatially Periodic Shear," J. Geophys. Res., **106**(C4), pp. 7027–7037.

[22] Fernandes, A. M., and Krishnamurti, R., 2010, "Salt Finger Fluxes in a Laminar Shear Flow," J. Fluid Mech., **658**, pp. 148–165.

[23] Hage, E., and Tilgner, A., 2010, "High Rayleigh Number Convection With Double Diffusive Fingers," Phys. Fluids, **22**(7), p. 076603.

[24] Yang, Y., Verzicco, R., and Lohse, D., 2016, "From Convection Rolls to Finger Convection in Double-Diffusive Turbulence," Proc. Natl. Acad. Sci. U. S. A., **113**(1), pp. 69–73.

[25] Balmforth, N. J., Ghadge, S. A., Kettapun, A., and Mandre, S. D., 2006, "Bounds on Double-Diffusive Convection," J. Fluid Mech., **569**, pp. 29–50.

[26] Yang, Y., Verzicco, R., and Lohse, D., 2016, "Vertically Bounded Double Diffusive Convection in the Fingering Regime: Comparing No-Slip Versus Free-Slip Boundary Conditions," Phys. Rev. Lett., **117**(18), p. 184501.

[27] Zonta, F., and Soldati, A., 2018, "Stably Stratified Wall-Bounded Turbulence," ASME Appl. Mech. Rev., **70**(4), p. 040801.

[28] Zonta, F., and Soldati, A., 2014, "Effect of Temperature Dependent Fluid Properties on Heat Transfer in Turbulent Mixed Convection," ASME J. Heat Trans., **136**(2), p. 022501.

[29] Yang, Y., Poel, E. P. V. D., Ostilla-Mónico, R., Sun, C., Verzicco, R., Grossmann, S., and Lohse, D., 2015, "Salinity Transfer in Bounded Double Diffusive Convection," J. Fluid Mech., **768**, pp. 476–491.